





# Asymmetric Character of the Ferroelectric Phase Transition and Charged Domain Walls in a Hybrid Improper Ferroelectric

## Journal Article

### Author(s):

Weber, Mads C.; Zemp, Yannik; [Trassin, Morgan](#) ; [Simonov, Arkadiy](#) ; Schaab, Jakob; Gao, Bin; Cheong, Sang-Wook; [Lottermoser, Thomas](#) ; [Fiebig, Manfred](#) 

### Publication date:

2022-06

### Permanent link:

<https://doi.org/10.3929/ethz-b-000505453>

### Rights / license:

[Creative Commons Attribution 4.0 International](#)

### Originally published in:

Advanced Electronic Materials 8(6), <https://doi.org/10.1002/aelm.202100434>

### Funding acknowledgement:

188414 - Multifunctional oxide electronics using natural ferroelectric superlattices (SNF)

178825 - Dynamical processes in systems with strong electronic correlations (SNF)

694955 - In-situ second harmonic generation for emergent electronics in transition-metal oxides (EC)

# Asymmetric Character of the Ferroelectric Phase Transition and Charged Domain Walls in a Hybrid Improper Ferroelectric

Mads C. Weber,\* Yannik Zemp, Morgan Trassin, Arkadiy Simonov, Jakob Schaab, Bin Gao, Sang-Wook Cheong, Thomas Lottermoser, and Manfred Fiebig

In improper ferroelectrics, the spontaneous ordering is typically driven by a structural distortion or a magnetic spin alignment. The induced electric polarization is only a secondary effect. This dependence is a rich source for unusual phenomena and ferroelectric domain configurations for proper, polarization-driven ferroelectrics. This study focuses on the polar domain structure and the hysteretic behavior at the ferroelectric phase transition in  $\text{Ca}_3\text{Mn}_{1.9}\text{Ti}_{0.1}\text{O}_7$  as a representative of the recently discovered hybrid improper ferroelectric class of multiferroics. Combining optical second harmonic generation and Raman spectroscopy gives access to the spontaneous structural distortion and the resulting improper electric polarization. This study shows that hybrid improper ferroelectrics contrast proper and improper ferroelectrics in several ways. Most intriguingly, adjacent ferroelectric domains favor head-to-head and tail-to-tail domain walls over charge-neutral configurations. Furthermore, the phase transition occurs in an asymmetric fashion. The regime of phase coexistence of the nonpolar and polar phases shows a clear and abrupt upper temperature limit. In contrast, the coexistence toward low temperatures is best described as a fade-out process, where 100-nm-sized islands of the nonpolar phase expand deep into the polar phase.

taneous polarization. In ferroelectric memory devices, domains can be considered as logic bits in which the polarization direction represents a binary information. The domains are separated by domain walls, which themselves may add further functionalities because they can possess non-bulk-like properties. These properties depend strongly on the crystallographic orientation of the walls. For instance, if the spontaneous polarization in neighboring ferroelectric domains points perpendicular to the domain wall,<sup>[1,2]</sup> so-called head-to-head or tail-to-tail walls form. These configurations can lead to a non-bulk-like conductivity of the domain walls because of charge-screening effects.<sup>[2]</sup>

Understanding and controlling the configuration of the domains is at the heart of functionalizing ferroelectrics. The criteria that determine this configuration strongly depend on the origin of the ferroelectric state. In proper ferroelectrics, where the polarization represents the primary order parameter, the domains typically arrange such that the energetically costly

head-to-head or tail-to-tail walls are avoided. In improper ferroelectrics, however, where the polarization is only a byproduct of another, leading order, other criteria are driving the domain formation. Therefore, improper ferroelectrics are an abundant source for unconventional domain structures.<sup>[3–7]</sup>

A novel contribution to this class of materials are the so-called hybrid improper ferroelectrics. Here, the ferroelectric state originates from two modes with different symmetries. These modes are not polar themselves. In their combination, however, they activate an electric polarization; hence the denomination as hybrid improper ferroelectric.<sup>[8]</sup>


Much research on hybrid improper ferroelectrics focuses on compounds like  $(\text{Ca},\text{Sr})_3(\text{Ti},\text{Mn})_2\text{O}_7$ . These compounds crystallize in a Ruddlesden–Popper structure built from double perovskite-type layers separated by rock-salt-like  $(\text{Ca},\text{Sr})\text{O}$  sheets (**Figure 1a**).<sup>[8,9]</sup> A plethora of tilt systems of the  $(\text{Ti},\text{Mn})\text{O}_6$  octahedra as central building blocks of this structure gives rise to a rich phase diagram of competing states.<sup>[10–15]</sup> While structural analyses based on X-ray and neutron diffraction were applied to a large variety of compounds of the  $(\text{Ca},\text{Sr})_3(\text{Ti},\text{Mn})_2\text{O}_7$ -family, investigations of the domain structure were mostly restricted to the titanium-rich compounds. Here, studies bring domain configurations with

## 1. Introduction

Ferroelectric functionalities are tightly bound to domains, that is, regions with different, yet uniform direction of the spon-

M. C. Weber, Y. Zemp, M. Trassin, A. Simonov, J. Schaab, T. Lottermoser, M. Fiebig  
Department of Materials  
ETH Zurich  
Zurich 8093, Switzerland  
E-mail: mads.weber@univ-lemans.fr

B. Gao, S.-W. Cheong  
Rutgers Center for Emergent Materials and Department of Physics  
and Astronomy  
Rutgers University  
Piscataway, NJ 08854, USA

 The ORCID identification number(s) for the author(s) of this article can be found under <https://doi.org/10.1002/aelm.202100434>.

© 2021 The Authors. Advanced Electronic Materials published by Wiley-VCH GmbH. This is an open access article under the terms of the Creative Commons Attribution License, which permits use, distribution and reproduction in any medium, provided the original work is properly cited.

DOI: 10.1002/aelm.202100434

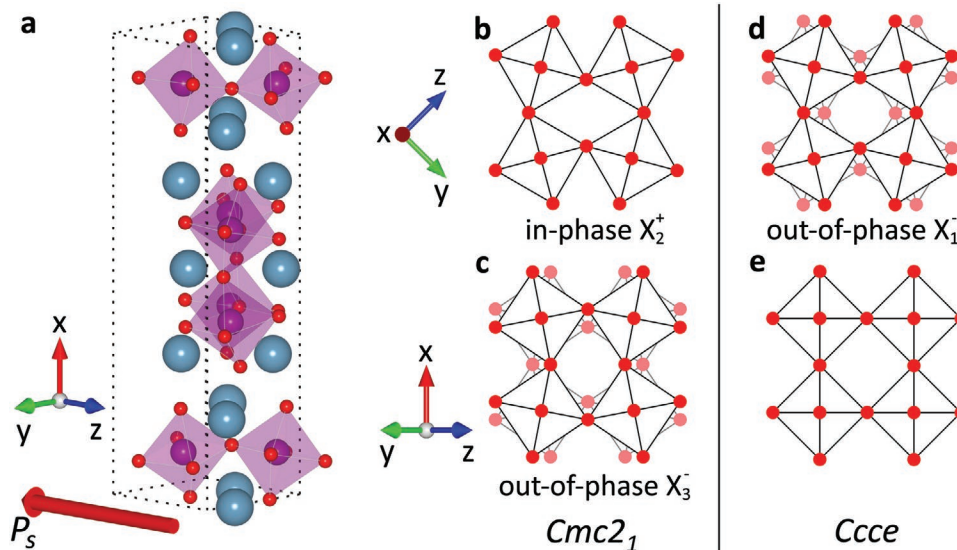


**Figure 1.** a) Ruddlesden–Popper crystal structure of  $\text{Ca}_3\text{Mn}_{1.9}\text{Ti}_{0.1}\text{O}_7$  in the polar room-temperature space group  $Cmc2_1$ . The red arrow indicates the direction of spontaneous polarization  $P_s$ . The calcium, manganese, and oxygen atoms are given in turquoise, violet, and red, respectively. Rotations of the octahedra in the  $Cmc2_1$  phase: b) in-phase rotation  $a^0a^0b^+$  around the fourfold axis of the tetragonal prototype phase; c) out-of-phase rotation  $a^-a^-b^0$  around the fourfold axis of the tetragonal prototype phase, d) rotate out-of-phase  $a^0a^0b^-$  around the fourfold axis of the tetragonal prototype phase, e) show no tilting around the  $x$  axes of the tetragonal prototype phase. The coordinate systems refer to the respective orthorhombic space groups.

intriguing features to light, such as conductive domain walls, anti-phase boundaries, and topological  $Z_4$  pseudo-vortex structures, where four domains with consecutive tilt pattern meet in a spatial singularity.<sup>9,13,16</sup>

In the manganese-rich compounds, however, attempts to visualize ferroelectric domains have been unsuccessful so far. Leakage currents impede piezo-response or conductive force microscopy.<sup>10,17</sup>

This is particularly unfortunate since the manganese-rich compounds exhibit magnetic order on top of the ferroelectric order.<sup>115,18</sup> Therefore, they belong to the class of multiferroics, which are of great current interest for their potential magnetoelectric functionality. Before this aspect can be addressed any further, we must first gain an understanding of the ferroelectric state and its domains.

In the present work, we therefore investigate the domain configuration in the manganese-rich hybrid improper ferroelectric  $\text{Ca}_3\text{Mn}_{1.9}\text{Ti}_{0.1}\text{O}_7$  with a focus on the role of the ferroelectric phase transition. We can only get to these results through a combination of experimental techniques, namely optical second harmonic generation (SHG) and Raman spectroscopy (RS). SHG, that is, frequency doubling of a light wave in a material, is extremely sensitive to the loss of inversion symmetry and thus a probe for emerging ferroelectricity.<sup>3,19,20</sup> RS is based on the inelastic scattering of light and is an excellent technique for probing tilt-driven phase transitions<sup>21</sup> and subtle structural distortions.<sup>22</sup> With the sensitivity of SHG and RS to polar and distortive properties, respectively, we gain access to structurally driven ferroelectricity and the associated domain structure.

We find that the ferroelectric behavior in hybrid improper ferroelectrics can contrast not only proper but also other improper ferroelectrics. Specifically, the polar  $180^\circ$  domains in  $\text{Ca}_3\text{Mn}_{1.9}\text{Ti}_{0.1}\text{O}_7$  prefer head-to-head and tail-to-tail rather than charge-neutral domain walls. Furthermore, the ferroelectric

phase transition shows an asymmetric character. While the phase coexistence of the nonpolar and polar phases has a clear upper temperature limit  $T_C^+$ , the region of phase coexistence expands far below  $T_C^+$  without a clear lower temperature limit.

## 2. Results and Discussion

### 2.1. Ferroelectric Phase Transition

The prototype space-group symmetry of  $\text{Ca}_3\text{Mn}_{1.9}\text{Ti}_{0.1}\text{O}_7$  is tetragonal,  $I4/mmm$ . From this, a phase transition to the orthorhombic  $Ccce$  phase takes place at, presumably, 1100 K.<sup>11,15,23</sup> It consists of an anti-phase rotation of the oxygen octahedra of  $X_1$  symmetry around the former fourfold axis of the tetragonal prototype phase<sup>11</sup> (Figure 1d,e; tilt system:  $a^0a^0b^-$  in Glazer's notation<sup>24</sup>). Subsequently, a first-order phase transition from the nonpolar  $Ccce$  to the polar  $Cmc2_1$  phase takes place at 364 and 380 K in cooling and heating runs, respectively.<sup>11,18,23</sup> The associated  $a^-a^-b^+$  tilt system of the octahedra is intriguing since it is composed of two nonpolar modes, that is, an in-phase rotation mode  $X_2^+$  ( $a^0a^0b^+$ ; Figure 1b) and an anti-phase rotation mode  $X_3^-$  ( $a^-a^-b^0$ ; Figure 1c).<sup>18</sup> In their combination, these modes activate a spontaneous electric polarization through  $\text{Ca}^{2+}$  displacement along the  $z$  direction (Figure 1a). A mechanism of this type is termed hybrid improper ferroelectricity.<sup>18</sup>

We now aim to understand the ferroelectric phase transition from a microscopic perspective. We begin by investigating the transition between the  $Ccce$  and  $Cmc2_1$  phases in SHG measurements. Centrosymmetric phases like  $Ccce$  do not allow for the leading-order all-electric-dipole-type SHG process. Phases without inversion symmetry, however, such as the polar  $Cmc2_1$  state permit this contribution (for further information see Supporting Information 3). **Figure 2a** shows

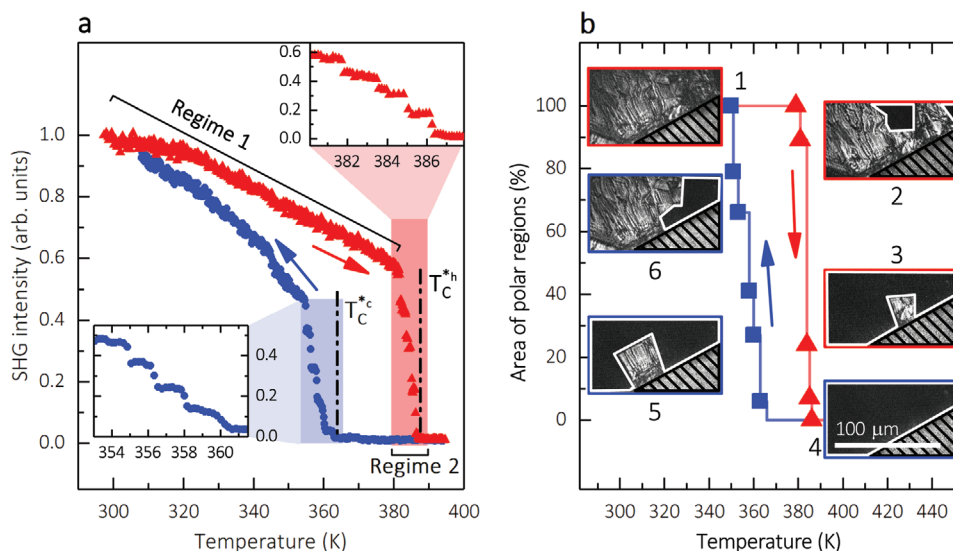


**Figure 2.** a) Evolution of the SHG signal with temperature across the hybrid improper ferroelectric phase transition (heating: red triangles; cooling: blue circles) measured at an SHG energy of 2.68 eV. The transition is characterized by two regimes. Regime 1: continuous change in signal. Regime 2: sequence of abrupt changes in signal (see zoom-in).  $T_C^*$ ,  $T_{C\text{-heating}}^*$  and  $T_{C\text{-cooling}}^*$  define the temperatures of zero SHG signal for heating and cooling runs, respectively. b) SHG microscopy images across Regime 2 illustrating the disappearance and re-appearance of the polar  $Cmc2_1$  phase in percent of the area of the images. Images 1 to 4 and 4 to 6 show the heating and cooling processes, respectively. Bright and dark regions identify the  $Cmc2_1$  and  $Ccce$  phases, respectively, with the phase boundaries outlined in white. The hatched area on the bottom right results from light scattered by silver paint glue. For a more detailed image series refer to Supporting Information 3.2.

the temperature-dependent SHG signal across the phase transition. In a heating run above room temperature, the SHG signal first declines to about 50% in a continuous fashion (Regime 1). At  $T_{C\text{-heating}}^* = 387$  K, the SHG signal shows a kink and vanishes in a staircase-like descent across a range of 3 K (Regime 2). During re-cooling, the inverse process takes place, yet now with  $T_{C\text{-cooling}}^* = 358$  K. The pronounced hysteresis with a width of 30 K confirms the first-order nature of the transition.<sup>[18,23]</sup> In Figure 2b, we track the hysteretic behavior by spatially resolved SHG imaging. We find that a Barkhausen-like transition of clearly demarcated sample areas causes the staircase-like progression of the SHG signal in Regime 2. The sequence of abrupt changes is likely caused by pinning of domain walls at defects, for example, of tilt pattern faults. Furthermore, the discontinuous nature of this first-order phase transition may play a role: The change between the out-of-phase tilts  $a^0a^0b^-$  in the  $Ccce$  phase and the in-phase tilts  $a^0a^0b^+$  in the  $Cmc2_1$  phase requires every second octahedron along the  $z$  direction of the tetragonal prototype phase to change its sense of rotation. The associated major atomic displacement might be particularly susceptible to structural inhomogeneities resulting in pinning effects.

Let us now turn to the pronounced, yet continuous change of the SHG signal with temperature in Regime 1. Two different scenarios may be responsible for the observed evolution: an extended region of phase coexistence of the nonpolar  $Ccce$  phase and the polar  $Cmc2_1$  phase below  $T_C^*$  (Scenario 1) or a conventional thermal decrease of the spontaneous polarization toward  $T_C^*$  (Scenario 2). In the former case, the change in signal would point to a change of the volume of the polar phase rather than of the polarization itself.

To identify if one of these options prevails or if both contribute to the signal change in Regime 1, we perform tem-

perature-dependent micro-RS. For Scenario 1, the phase coexistence, the Raman spectra of both phases would be detected simultaneously but both spectral contributions would exhibit different evolutions with temperature.<sup>[25]</sup> For Scenario 2, the change in polarization, one would expect a change of the vibrational frequencies of the tilt modes, which couple linearly to the ferroelectric mode.<sup>[8]</sup>

Figure 3a shows the temperature-dependent Raman spectra during a heating run (for the selection rules of the Raman-active modes refer to Supporting Information 2). At 298 and 413 K, we find a spectral dependence that is characteristic for the  $Cmc2_1$  and the  $Ccce$  phase, respectively.<sup>[26]</sup> The two spectra differ significantly in number and frequencies of the observed modes. In a heating run, the signal of the  $Ccce$  phase gives rise to new spectral features complementing the spectral signature of the  $Cmc2_1$  phase (see Figure 3a, green shaded areas). With further increasing temperature, the contribution of the  $Ccce$  phase to the spectrum increases until at  $T_{C\text{-heating}}^* = 390$  K, analogous to the SHG data, the sample abruptly transfers into the pure  $Ccce$  phase. We therefore find a substantial temperature interval of phase coexistence in Regime 1 in agreement with Scenario 1.  $T_{C\text{-heating}}^*$  as transition temperature marks the limit of the polar  $Cmc2_1$  phase and, hence, the high-temperature boundary of the region of phase coexistence.

Figure 3b illustrates this evolution by the normalized weight of both spectra extracted from their fits. For the spectral features of the  $Ccce$  phase, converging fits are obtained starting from at 358 K. We therefore show the data points down to this value, even though the region of phase coexistence is likely to extend to even lower temperature. Note that the normalized weight of the spectral intensity is no measure for the volumetric ratio of the two phases since their scattering probabilities are most likely different.

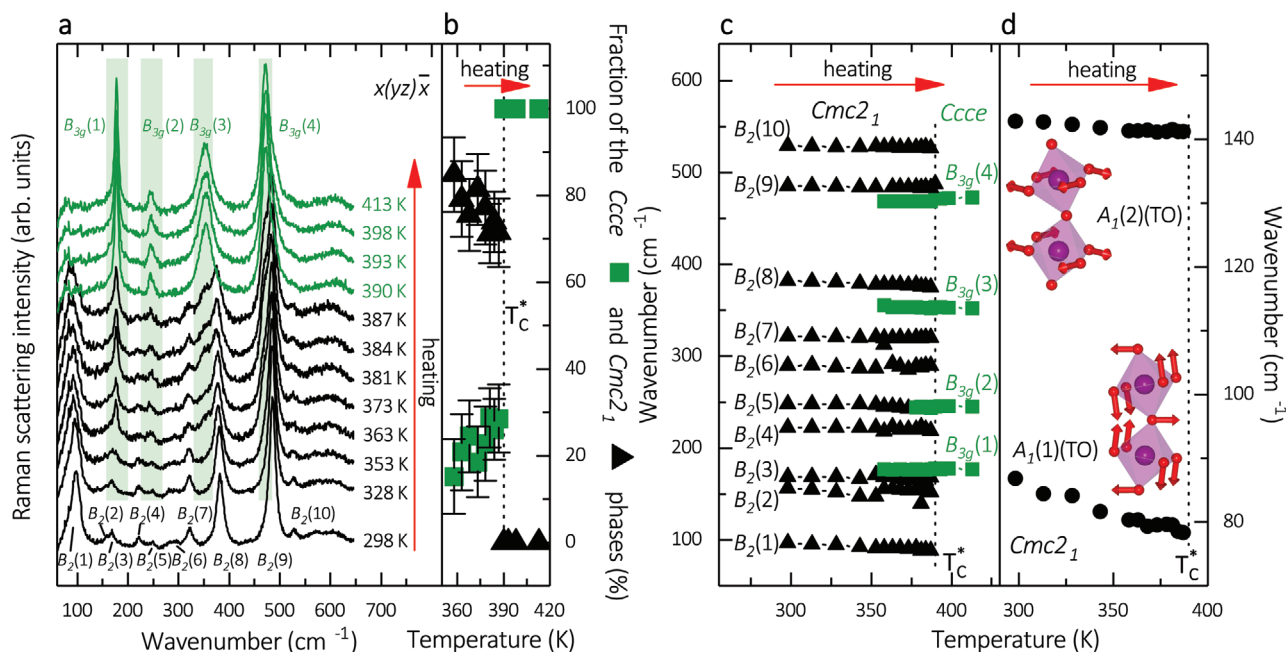


**Figure 3.** a) Evolution of the Raman spectra in  $x(yz)\bar{x}$  configuration (for further information on the Raman selection rules see Supporting Information 2) with increasing temperature across the phase transition. The spectra of the *Ccce* and of the (predominantly) *Cmc*<sub>21</sub> phase are given in green and black, respectively. Emergent spectral features of the nonpolar phase within the polar phase are shaded green. b) Onset and decline of the *Ccce* (green squares) and *Cmc*<sub>21</sub> (black triangles) phases, respectively, as normalized weight of the spectra. c) Evolution of the B<sub>3g</sub> (*Ccce*, green squares) and B<sub>2</sub>(TO) (*Cmc*<sub>21</sub>, black triangles) mode frequencies with increasing temperatures (see Supporting Information 2.1 for the evolution of the A<sub>1</sub>(TO) modes). d) Evolution of the frequencies of the A<sub>1</sub>(TO) soft modes in the *Cmc*<sub>21</sub> phase. As illustrated, the vibrational patterns of the soft modes relate directly to the in-phase and out-of-phase tilts of the octahedra that represent the order parameters of the system. The dotted lines in (b–d) mark T<sub>C</sub><sup>heating</sup>.

We estimate the size of the inclusions of the *Ccce* phase below T<sub>C</sub><sup>\*</sup> to be in the 100-nm range because with a spot size of the Raman probe of 1 μm, we already obtain a homogeneous Raman signal throughout the sample. Note that to identify this hierarchical structure of large ferroelastic domains with embedded tens-of-micrometer-sized ferroelectric domains, which are infused by nanometric nonpolar islands, we need the combination of both SHG measurements and RS. Because of the substantially smaller laser spot size of Raman measurements in comparison with SHG measurements (270 μm), the staircase-like transition process of Regime 2 is not observed in the former. From the SHG measurements in Figure 2a, we find that aside from the hysteretic temperature shift of T<sub>C</sub><sup>\*</sup> the behavior in heating and cooling runs is the same.

In the next step, we examine if the phase coexistence (Scenario 1) alone is responsible for the temperature dependence of the SHG signal in Regime 1, or if a change in polarization also plays a role (Scenario 2). Figure 3c shows the temperature-dependent evolution of the phonon-mode frequencies extracted from Figure 3a. We find that the modes show no sign of softening toward T<sub>C</sub><sup>heating</sup>. To access the (Ti,Mn)O<sub>6</sub> tilt angles, which are proportional to the polar displacement, we trace the tilt vibrations toward T<sub>C</sub><sup>heating</sup>. Thanks to a recent mode assignment,<sup>[26]</sup> we identify the A<sub>1</sub>(TO) modes at 142 and 87 cm<sup>-1</sup> as in-phase and out-of-phase tilt modes, respectively. Figure 3d shows the evolution of both modes with rising temperature. Between room temperature and T<sub>C</sub><sup>heating</sup>, the in-phase rotation mode (142 cm<sup>-1</sup>) exhibits a shift by 1 cm<sup>-1</sup>. The out-of-phase rotation mode (87 cm<sup>-1</sup>) shifts by 8 cm<sup>-1</sup>. Making use of the linear

relation between the vibrational frequency and the tilt angle (the magnitude of the order parameter is approximately proportional to the frequency of the associated mode<sup>[27,28]</sup>), and by comparison with neutron diffraction data,<sup>[18]</sup> we can approximate the tilt-related frequency shifts as 171 and 12.5 cm<sup>-1</sup> deg<sup>-1</sup> for the in-phase and the out-of-phase rotations, respectively. This is in good agreement with data obtained for the related perovskite-type compounds CaTiO<sub>3</sub><sup>[29]</sup> and CaMnO<sub>3</sub>.<sup>[30,31]</sup> With about 0.06°, the modification of the angle of the in-phase rotation mode is therefore negligible. For the out-of-phase rotation, we estimate a rotation change of about 0.6°, in good agreement with neutron diffraction data.<sup>[18]</sup> This corresponds to a change of the out-of-phase rotation by 10%. Therefore, the related change in polarization is minor in comparison to the one at proper ferroelectric phase transitions, which is also consistent with reports by Senn and co-workers.<sup>[11]</sup> With the relation  $P_s \propto E(2\omega) \propto I_{\text{SHG}}^{1/2}$ ,<sup>[3]</sup> where  $P_s$  is the spontaneous polarization of the material and  $E(2\omega)$  and  $I_{\text{SHG}}$  are the electric field and intensity of the SHG light, respectively, the polarization change thus can only account for 20% of the variation of the SHG signal in Regime 1.

We therefore conclude that the polarization (Scenario 2) change plays a secondary role in Regime 1, which is instead dominated by a wide region of phase coexistence (Scenario 1) below T<sub>C</sub><sup>\*</sup>. In an asymmetric fashion, this phase coexistence prevails below T<sub>C</sub><sup>\*</sup> only. The crystalline structure remains rigid around the phase transition at T<sub>C</sub><sup>\*</sup>. The transition is, therefore, best described as an abrupt event, during which the in-phase tilts (*a*<sup>0</sup>*a*<sup>0</sup>*b*<sup>+</sup>, *Cmc*<sub>21</sub>) transfer into out-of-phase tilts (*a*<sup>0</sup>*a*<sup>0</sup>*b*<sup>-</sup>, *Ccce*

phase), with every second octahedron changing the sense of rotation. This contrasts with typical proper ferroelectric phase transitions, like in  $\text{BaTiO}_3$ , which exhibit a softening of the order-parameter-related mode and of the associated polarization close to the phase transition.<sup>[32]</sup> Although the evolution of the SHG signal across the ferroelectric transition in  $\text{BaTiO}_3$  and  $\text{Ca}_3\text{Mn}_{1.9}\text{Ti}_{0.1}\text{O}_7$  is therefore similar at first glance, their microscopic origin is very different.<sup>[33]</sup>

## 2.2. Ferroelastic and Ferroelectric Domain Configuration

We now scrutinize the domain configuration in the ferroelectric phase. With  $I4/mmm$  as prototype symmetry, the  $Cmc2_1$  phase has two ferroelastic domain states with mutually exchanged  $y$  and  $z$  axes. Each of these hosts two ferroelectric domain states with opposite direction of the spontaneous polarization parallel to the  $z$  axes, giving rise to four polarization domain states in total. (For an in-depth discussion of the resulting domain-wall configurations see Ref. [9].)

First, we image the ferroelastic domains by RS. We use the differences in the signatures of the Raman spectra for differently oriented ferroelastic domains to map the domain configuration (see Supporting Information 2.2). Since every image point represents an entire spectrum, this method, unlike photographic microscopy techniques, is very robust against intensity changes due to surface imperfections. **Figure 4a** shows the domain configuration as a distribution of bright and dark regions representing the two ferroelastic domain states, to which we refer as FA-1 and FA-2. The ferroelastic domains are  $\approx 100 \mu\text{m}$  in size, comparable to earlier findings.<sup>[23]</sup> To identify the orientation of the polar axis within the ferroelastic domains, we measure the anisotropy of the SHG signal (see Supporting Information 3.1). In accordance with the allowed SHG tensor components in the  $Cmc2_1$  space group (Supporting Information 3), we find as expected the polar axes in FA-1 and FA-2 perpendicular to each other as indicated in **Figure 4a**. Hence, the ferroelastic domain walls roughly align with  $x$  and  $y$  axes of the tetragonal prototype phase, which are oriented at  $45^\circ$  to the orthorhombic  $y$  and  $z$  axes.

In the next step, we investigate the ferroelectric  $180^\circ$  domains within the ferroelastic domains by spatially resolved SHG imaging. **Figure 4b** shows the SHG image of the center part of **Figure 4a** with FA-1 and FA-2 appearing as bright and dark, respectively (for a visualization of FA-2 see Supporting Information 3.3). The ferroelastic domain configurations obtained by SHG and RS imaging are in striking agreement. This agreement of the reflection-based SHG image and the spectrum-based RS image allows us to exclude optical artifacts in the SHG images. For example, areas of altered surface roughness, which therefore emit reduced SHG intensity could be falsely interpreted as different ferroelastic domain, but the spectrum-based RS imaging allows for the unambiguous identification of the domain state. Within the probed FA-1 area, we observe regions of different brightness. These results from domains stacked parallel to the surface so that the passing laser beam leads to interfering SHG contributions.

Furthermore, we identify black lines within  $yz$  plane. The lines result from the destructive interference occurring at the boundary between the ferroelectric domains and hence

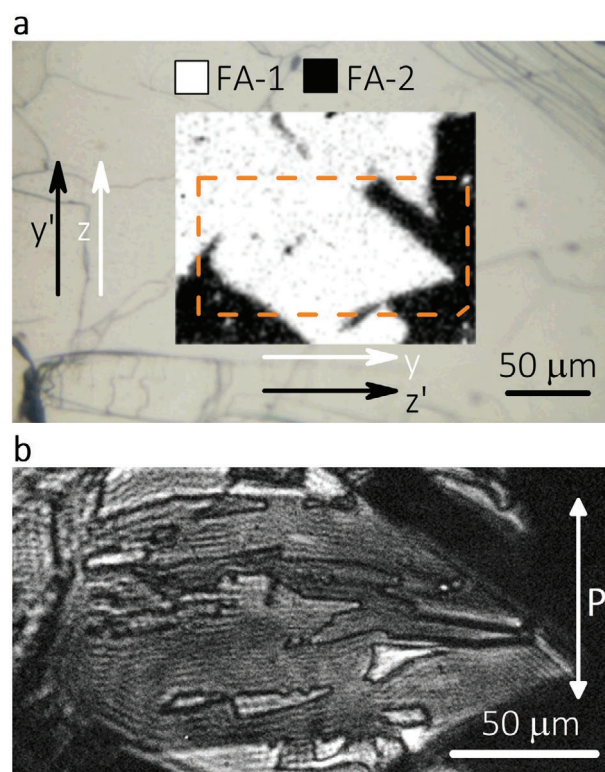


**Figure 4.** a) RS imaging map of the ferroelastic domains (FA-1 and FA-2) in  $\text{Ca}_3\text{Mn}_{1.9}\text{Ti}_{0.1}\text{O}_7$  superimposed onto a white-light image of the sample. The domain shape was extracted via principle component analysis from spectra measured for each image point (see Supporting Information 2.2). The white and black arrows indicate the crystallographic orientations of FA-1 and FA-2, respectively. The directions were derived from SHG measurements (see Supporting Information 3.1). b) SHG image of the region outlined by the dashed orange box in (a). Ferroelastic domain walls are in excellent agreement with (a). The black lines indicated the position of  $180^\circ$  ferroelectric domain walls. The arrow indicates the directions of the spontaneous polarization of the ferroelectric domains in FA-1.

indicate the position of the ferroelectric  $180^\circ$  domain walls near the surface.<sup>[34]</sup> The ferroelectric domains have a lateral extension on the order of tens of micrometers. This is comparable to the lateral expansion observed in the related compound  $\text{Ca}_3\text{Ti}_2\text{O}_7$ .<sup>[9,35]</sup>

For clarity, **Figure 5a** illustrates the distribution of the different domain and domain-wall types. To describe the relation between a ferroelectric domain wall and the direction of the spontaneous polarization, we introduce the angle  $\theta$  as defined in **Figure 5a**.  $\theta = 0^\circ, 180^\circ$  means that the domain walls are oriented parallel to the polarization and are thus electrically neutral. For  $\theta = 90^\circ$  and  $270^\circ$ , the domain walls are perpendicular to the polarization, indicating charged head-to-head and tail-to-tail walls, respectively. In **Figure 5b**, we show the integrated length of the domain walls against the angle  $\theta$ . Strikingly, the domain walls preferentially align perpendicular to the local polar axis as indicated by the maxima for  $\theta = 90^\circ$  and  $270^\circ$ . In other words,  $\text{Ca}_3\text{Mn}_{1.9}\text{Ti}_{0.1}\text{O}_7$  favors maximal head-to-head and tail-to-tail walls over neutral walls.

This is a remarkable and very unexpected observation. In proper ferroelectrics, such as  $\text{Pb}(\text{Zr,Ti})\text{O}_3$ ,  $\text{LiNbO}_3$ , or

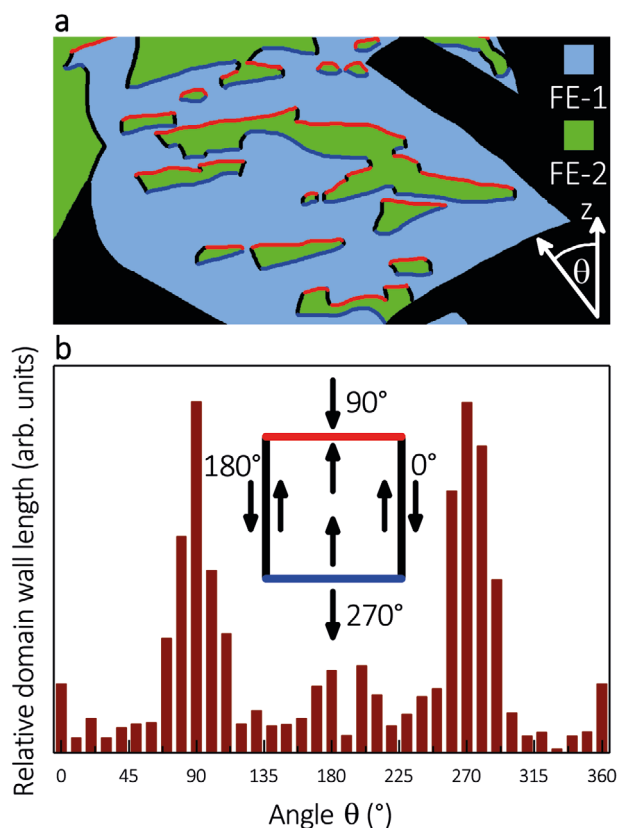


**Figure 5.** a) Sketch of Figure 4b as guide to the eye on the different types of domain walls. Light blue and light green areas identify different types of ferroelectric domain states, FE-1 and FE-2, within FA-1. Black, red, and blue refer to neutral, head-to-head, and tail-to-tail domain walls, respectively. b) Relative domain wall length with respect to the angle  $\theta$  between the spontaneous polarization and the domain-wall orientation. 0° and 180° refer to neutral walls, 90° to head-to-head, and 270° to tail-to-tail walls.

BiFeO<sub>3</sub>, charged domain walls are avoided because of the resulting Coulomb forces and the energetic costs for their screening. Hence, charged domain walls usually occur only through strain, in thin films, by poling or as slightly inclined walls.<sup>[2,36–38]</sup> In improper ferroelectrics, the tendency to avoid head-to-head and tail-to-tail walls is less dominant.<sup>[4,6,9,39,40]</sup> Hybrid improper ferroelectrics further detach from this guideline. In the related compounds (Ca,Sr)<sub>3</sub>Ti<sub>2</sub>O<sub>7</sub>, the Coulomb forces appear insignificant with domain walls forming arbitrarily angles of 0°, 45°, 90°, 135°, etc. with the polarization to avoid distortions of the octahedra. Ca<sub>3</sub>Mn<sub>1.9</sub>Ti<sub>0.1</sub>O<sub>7</sub> even goes to the extreme and prefers a domain configuration with charged head-to-head (90°) and tail-to-tail walls (270°) in the as-grown state.

The explicit preference for the ferroelectric head-to-head and tail-to-tail walls is likely linked to the layered structure. For instance, out-of-phase boundaries that are structural defects inherent to the layered perovskite-type materials lead to charge accumulations as reported for Aurivillius-type compounds.<sup>[41]</sup> The stabilization of head-to-head and tail-to-tail walls may compensate for these defects and be energetically favorable despite their nominally charged character.

### 3. Conclusion

Using the unique combination of SHG measurements and Raman spectroscopy, we observe an unusual phase transition between the nonpolar *Cccc* and the polar *Cmc2<sub>1</sub>* phases in the hybrid improper ferroelectric material Ca<sub>3</sub>Mn<sub>1.9</sub>Ti<sub>0.1</sub>O<sub>7</sub>. This phase transition is characterized by a highly asymmetric behavior of phase coexistence. While there is a clear upper temperature boundary  $T_C^*$  of the phase coexistence of the *Cccc* and *Cmc2<sub>1</sub>* phases, there is no such boundary toward the low temperature side. 100-nm-sized islands of the nonpolar phase expand deep into the polar phase. These nonpolar inclusions within the polar phase may be the reason why the ferroelectric poling was so far observed at cryogenic temperatures only.<sup>[17]</sup> This behavior contrasts most proper and improper ferroelectrics, where the switching is easiest close to the Curie temperature.

Furthermore, the ferroelectric domains favor a counterintuitive formation of head-to-head and tail-to-tail boundaries even in the as-grown state. This typically avoided configuration is a source for charged domain walls with a conductivity substantially different from the bulk. The charged, possibly conductive domain walls in combination with the in-plane ferroelectricity and the layered structure of Ca<sub>3</sub>Mn<sub>1.9</sub>Ti<sub>0.1</sub>O<sub>7</sub> make this compound very promising for the functionalization of ferroelectrics. In particular, a recent study showed that layered perovskite-type ferroelectrics can be switched fatigue free.<sup>[42]</sup>

Unlike other hybrid improper ferroelectrics, Ca<sub>3</sub>Mn<sub>1.9</sub>Ti<sub>0.1</sub>O<sub>7</sub> also exhibits magnetic order. The combination of magnetism and uncommon ferroelectric behavior may open up perspectives for unusual magnetoelectric coupling phenomena in hybrid improper ferroelectrics. Just like the ferroelectric order, the magnetic order is linked to the tilts of the octahedra. Therefore, the magnetic domains must follow the same domain hierarchy as the ferroelectric domains – forming 90° walls with ferroelastic walls and magnetic 180° walls only interior ferroelastic domains.

### 4. Experimental Section

Ca<sub>3</sub>Mn<sub>1.9</sub>Ti<sub>0.1</sub>O<sub>7</sub> crystals were grown by the floating-zone method as described elsewhere.<sup>[23]</sup> We perform SHG and RS experiments on a single-crystalline sample in near-normal or normal incidence to the optically flat cleavage planes, which lie orthogonal to the *x* axis, as confirmed by single-crystal X-ray diffraction.

For our SHG measurements, we used a Coherent Elite Duo laser system (central wavelength 800 nm, pulse width 125 fs, 8 mJ pulse energy, repetition rate 1 kHz) to pump an optical parametric amplifier, which, supplemented by frequency mixing stages, generates laser light between 0.41 and 4.96 eV. The polarization of the incident and the detected light was set by a half-wave plate and a Glan–Taylor prism, respectively. Long-pass filters were mounted in front of the sample to suppress higher harmonics generated in the optical components. Behind the sample, short-pass filters cut off the fundamental light. A photomultiplier tube detects the SHG light. Spectral resolution is provided by a monochromator. Alternatively, a long-working-distance microscope objective with a magnification of 20 and a liquid-nitrogen-cooled Jobin Yvon Back Illuminated Deep Depletion CCD camera were used to image the domain structure at a fixed photon energy with a spatial resolution of 1  $\mu$ m. A heating plate and a self-made furnace based on resistive heating allowed for measurements above room temperature.

An inVia Renishaw Reflex Raman microscope in micro-Raman mode with a 633-nm He-Ne laser and a spectral cut-off of  $70\text{ cm}^{-1}$  was used. During the RS experiments, crystals were heated using a Linkam THMS600 stage. We limited the laser power to reduce the sample heating to  $\leq 2\text{ K}$ . Intensities and frequencies of the phonon modes were obtained by fitting the Raman spectra with Lorentzian functions.

## Supporting Information

Supporting Information is available from the Wiley Online Library or from the author.

## Acknowledgements

The authors are grateful to J. Kreisel (University of Luxembourg) and I. Burgert and T. Keplinger (ETH Zurich) for allowing the use of Raman spectroscopy facilities. The authors thank T. Weber and the D-MATL X-Ray Service Platform for experimental support. This work was financially supported by SNSF (Grant No. 200021\_178825/1) and European Research Council (Advanced Grant 694955-INSEETO). M.T. acknowledges financial support by the Swiss National Science Foundation under Project 200021\_188414. A.S. acknowledges financial support through the SNF Ambizione PZ00P2\_180035 grant. The work at Rutgers University was supported by the DOE under Grant No. DOE: DE-FG02-07ER46382.

## Conflict of Interest

The authors declare no conflict of interest.

## Data Availability Statement

The data that support the findings of this study are available from the corresponding author upon reasonable request.

## Keywords

charged domain walls, hybrid improper ferroelectric, multiferroic, phase transition

Received: April 26, 2021

Revised: July 9, 2021

Published online:

- [1] D. Meier, *J. Phys.: Condens. Matter* **2015**, *27*, 463003.  
 [2] P. S. Bednyakov, B. I. Sturman, T. Sluka, A. K. Tagantsev, P. V. Yudin, *npj Comput. Mater.* **2018**, *4*, 65.  
 [3] M. Lilienblum, T. Lottermoser, S. Manz, S. M. Selbach, A. Cano, M. Fiebig, *Nat. Phys.* **2015**, *11*, 1070.  
 [4] D. Meier, J. Seidel, A. Cano, K. Delaney, Y. Kumagai, M. Mostovoy, N. A. Spaldin, R. Ramesh, M. Fiebig, *Nat. Mater.* **2012**, *11*, 284.  
 [5] T. Choi, Y. Horibe, H. T. Yi, Y. J. Choi, W. Wu, S.-W. Cheong, *Nat. Mater.* **2010**, *9*, 253.  
 [6] M. Matsubara, S. Manz, M. Mochizuki, T. Kubacka, A. Iyama, N. Aliouane, T. Kimura, S. L. Johnson, D. Meier, M. Fiebig, *Science* **2015**, *348*, 1112.  
 [7] D. Meier, M. Maringer, T. Lottermoser, P. Becker, L. Bohatý, M. Fiebig, *Phys. Rev. Lett.* **2009**, *102*, 107202.

- [8] N. A. Benedek, C. J. Fennie, *Phys. Rev. Lett.* **2011**, *106*, 107204.  
 [9] Y. S. Oh, X. Luo, F.-T. Huang, Y. Wang, S.-W. Cheong, *Nat. Mater.* **2015**, *14*, 407.  
 [10] F. Pomiro, C. Ablitt, N. C. Bristowe, A. A. Mostofi, C. Won, S.-W. Cheong, M. S. Senn, *Phys. Rev. B* **2020**, *102*, 014101.  
 [11] M. S. Senn, A. Bombardi, C. A. Murray, C. Vecchini, A. Scherillo, X. Luo, S.-W. Cheong, *Phys. Rev. Lett.* **2015**, *114*, 035701.  
 [12] M. S. Senn, C. A. Murray, X. Luo, L. Wang, F.-T. Huang, S.-W. Cheong, A. Bombardi, C. Ablitt, A. A. Mostofi, N. C. Bristowe, *J. Am. Chem. Soc.* **2016**, *138*, 5479.  
 [13] F.-T. Huang, B. Gao, J.-W. Kim, X. Luo, Y. Wang, M.-W. Chu, C.-K. Chang, H.-S. Sheu, S.-W. Cheong, *npj Quantum Mater.* **2016**, *1*, 16017.  
 [14] M. Kratochvilova, F.-T. Huang, M.-T. F. Diaz, M. Klicpera, S. J. Day, S. P. Thompson, Y.-S. Oh, B. Gao, S.-W. Cheong, J.-G. Park, *J. Appl. Phys.* **2019**, *125*, 244102.  
 [15] M. V. Lobanov, M. Greenblatt, E. a. N. Caspi, J. D. Jorgensen, D. V. Sheptyakov, B. H. Toby, C. E. Botez, P. W. Stephens, *J. Phys.: Condens. Matter* **2004**, *16*, 5339.  
 [16] F. T. Huang, F. Xue, B. Gao, L. H. Wang, X. Luo, W. Cai, X. Z. Lu, J. M. Rondinelli, L. Q. Chen, S. W. Cheong, *Nat. Commun.* **2016**, *7*, 11602.  
 [17] M. Liu, Y. Zhang, L.-F. Lin, L. Lin, S. Yang, X. Li, Y. Wang, S. Li, Z. Yan, X. Wang, X.-G. Li, S. Dong, J.-M. Liu, *Appl. Phys. Lett.* **2018**, *113*, 022902.  
 [18] F. Ye, J. Wang, J. Sheng, C. Hoffmann, T. Gu, H. J. Xiang, W. Tian, J. J. Molaison, A. M. dos Santos, M. Matsuda, B. C. Chakoumakos, J. A. Fernandez-Baca, X. Tong, B. Gao, J. W. Kim, S.-W. Cheong, *Phys. Rev. B* **2018**, *97*, 041112.  
 [19] T. Lottermoser, D. Meier, R. V. Pisarev, M. Fiebig, *Phys. Rev. B* **2009**, *80*, 100101.  
 [20] D. Meier, N. Leo, G. Yuan, T. Lottermoser, M. Fiebig, P. Becker, L. Bohatý, *Phys. Rev. B* **2010**, *82*, 155112.  
 [21] J. F. Scott, *Rev. Mod. Phys.* **1974**, *46*, 83.  
 [22] M. C. Weber, M. Guennou, N. Dix, D. Pesquera, F. Sánchez, G. Herranz, J. Fontcuberta, L. López-Conesa, S. Estradé, F. Peiró, J. Iñiguez, J. Kreisel, *Phys. Rev. B* **2016**, *94*, 014118.  
 [23] B. Gao, F.-T. Huang, Y. Wang, J.-W. Kim, L. Wang, S.-J. Lim, S.-W. Cheong, *Appl. Phys. Lett.* **2017**, *110*, 222906.  
 [24] A. M. Glazer, *Acta Crystallogr. B* **1972**, *28*, 3384.  
 [25] O. N. Shebanova, P. Lazor, *J. Raman Spectrosc.* **2003**, *34*, 845.  
 [26] A. Glamazda, D. Wulferding, P. Lemmens, B. Gao, S.-W. Cheong, K.-Y. Choi, *Phys. Rev. B* **2018**, *97*, 094104.  
 [27] W. Hayes, R. Loudon, *Scattering of Light by Crystals*, John Wiley & Sons, New York **1978**.  
 [28] M. C. Weber, M. Guennou, H. J. Zhao, J. Iñiguez, R. Vilarinho, A. Almeida, J. A. Moreira, J. Kreisel, *Phys. Rev. B* **2016**, *94*, 214103.  
 [29] M. Guennou, P. Bouvier, B. Krikler, J. Kreisel, R. Haumont, G. Garbarino, *Phys. Rev. B* **2010**, *82*, 134101.  
 [30] K. Poepplmeier, M. Leonowicz, J. Scanlon, J. Longo, W. Yelon, *J. Solid State Chem.* **1982**, *45*, 71.  
 [31] M. V. Abrashev, J. Bäckström, L. Börjesson, V. N. Popov, R. A. Chakalov, N. Kolev, R.-L. Meng, M. N. Iliev, *Phys. Rev. B* **2002**, *65*, 184301.  
 [32] A. von Hippel, *Rev. Mod. Phys.* **1950**, *22*, 221.  
 [33] K. J. Choi, M. Biegalski, Y. L. Li, A. Sharan, J. Schubert, R. Uecker, P. Reiche, Y. B. Chen, X. Q. Pan, V. Gopalan, L.-Q. Chen, D. G. Schlom, C. B. Eom, *Science* **2004**, *306*, 1005.  
 [34] M. Fiebig, D. Fröhlich, T. Lottermoser, M. Maat, *Phys. Rev. B* **2002**, *66*, 144102.  
 [35] M. H. Lee, C.-P. Chang, F.-T. Huang, G. Y. Guo, B. Gao, C. H. Chen, S.-W. Cheong, M.-W. Chu, *Phys. Rev. Lett.* **2017**, *119*, 157601.  
 [36] M. Schröder, A. Haußmann, A. Thiessen, E. Soergel, T. Woike, L. M. Eng, *Adv. Funct. Mater.* **2012**, *22*, 3936.  
 [37] J. Seidel, L. W. Martin, Q. He, Q. Zhan, Y.-H. Chu, A. Rother, M. E. Hawkrige, P. Maksymovych, P. Yu, M. Gajek,



- N. Balke, S. V. Kalinin, S. Gemming, F. Wang, G. Catalan, J. F. Scott, N. A. Spaldin, J. Orenstein, R. Ramesh, *Nat. Mater.* **2009**, *8*, 229.
- [38] C.-L. Jia, S.-B. Mi, K. Urban, I. Vrejoiu, M. Alexe, D. Hesse, *Nat. Mater.* **2008**, *7*, 57.
- [39] P. Chu, Y. L. Wang, L. Lin, S. Dong, J. M. Liu, *IEEE Trans. Magn.* **2013**, *49*, 3117.
- [40] N. Leo, A. Bergman, A. Cano, N. Poudel, B. Lorenz, M. Fiebig, D. Meier, *Nat. Commun.* **2015**, *6*, 6661.
- [41] M. Campanini, M. Trassin, C. Ederer, R. Erni, M. D. Rossell, *ACS Appl. Electron. Mater.* **2019**, *1*, 1019.
- [42] E. Gradauskaite, M. Campanini, B. Biswas, C. W. Schneider, M. Fiebig, M. D. Rossell, M. Trassin, *Adv. Mater. Interfaces* **2020**, *7*, 2000202.